

Simultaneous Multispectral Imaging of the Discrete Aurora

Joshua Semeter,¹ Dirk Lummerzheim,² and Gerhard Haerendel³

Abstract.

A unique multispectral imager and an associated multispectral analysis framework are described which together constitute a new diagnostic tool for auroral research. By acquiring spatial and spectral data simultaneously, multispectral imaging allows one to exploit physical connections between auroral morphology and the auroral optical spectrum in a way that sequential spectral imaging cannot. The initial research focus is on imaging the transition in the incident energy spectrum during the formation of discrete arcs - that is, when the precipitating population is characterized by <1 keV electrons. A technique is presented which uses two spectral bands (centered at 4278\AA and 7325\AA) to extend the effective dynamic range of passive imaging to much lower energies.

1. Introduction

The optical aurora provides two distinct windows into magnetospheric electrodynamics: (1) the spatial structure in the plane perpendicular to \mathbf{B} and (2) the optical spectrum. In the spatial dimension, large-scale auroral structures - such as spirals and folds - are a direct projection of magnetospheric dynamics, while small-scale structures - such as curls and filamentary aurora - project near-Earth electrodynamics and plasma instabilities [Hallinan, 1976]. The optical spectrum provides information about the energetic electrons associated with these structures. In the magnetic zenith, for example, the ratio of OI 6300\AA brightness to N_2^+ 4278\AA brightness has long been used as a proxy for the characteristic energy of the incident energy spectrum [Rees and Luckey, 1974]. This work concerns the physical connection between these complementary dimensions of auroral information.

Consider, for example, auroral curls. Although they are generally understood as a manifestation of a Kelvin-Helmholtz (KH) instability, quantitative comparisons with observed curl motions has been inconsis-

tent with this interpretation [Vogt *et al.*, 1999, and references therein]. The KH instability can arise from a shear in the $\mathbf{E} \times \mathbf{B}$ drift velocity created by the convergent electric field of an auroral arc. The magnitude of the shear is proportional to $\nabla \times (\mathbf{E} \times \mathbf{B}) \propto \partial E_{\perp} / \partial x$, with x perpendicular to the arc. For a curl-free field, the integral of E_{\perp} gives the parallel potential drop experienced by the arc-related electrons. The net potential drop is in turn reflected in the characteristic energy, which can be estimated from the optical spectrum. Thus, a combined spatial-spectral analysis would add valuable new constraints to studies of auroral plasma instabilities.

Because the discrete aurora is highly variable, a true multispectral analysis requires that the spatial and spectral data be acquired simultaneously. Typically, multispectral images are acquired sequentially using a monochromatic imager and a filter wheel, precluding true simultaneity. An imaging spectrograph provides simultaneous spectral information, but is of limited use in studying dynamic aurora because of the lack of two-dimensional spatial information. In this paper we describe a unique new instrument and an analysis framework for high-resolution multispectral studies of the discrete aurora. Developed in collaboration with the Max-Planck-Institut für Extraterrestrische Physik,

¹SRI International, Menlo Park, California.

²Geophysical Institute, University of Alaska, Fairbanks, Alaska

³International University, Bremen, Germany

the Simultaneous Multispectral Imager (SMI) images four discrete wavelengths through a single optical chain onto a single detector, with ~ 1 km spatial resolution at E -region altitudes and .3 to 10 s time resolution (depending on signal strength).

The initial scientific focus is on the study of low-energy (< 1 keV) precipitation in the discrete aurora. The importance of this energetic regime is discussed in Section 2, which describes some unexpected features observed in electron distribution functions over weak auroral arcs. Section 3 provides a review of the information in the auroral spectrum, suggesting the type of measurement required to study acceleration region dynamics at low energies. Section 4 describes the SMI and its current filter characteristics. Section 5 presents a specific analysis technique involving two spectral images: one centered at 4278\AA (N_2^+ First Negative), and the other at 7325\AA (mixture of N_2 First Positive and O^+ 7320\AA). Finally, Section 6 presents examples that demonstrate two applications of this technique: (1) to resolve the spatial-temporal ambiguity associated with changes in the incident energy spectrum and (2) to enhance the sensitivity and dynamic range of auroral imaging.

2. Relationship among number flux, energy flux, and luminosity

To appreciate the scientific efficacy of multispectral imaging, consider first the relationship between the electron energy spectrum and auroral luminosity. Studies of the aurora have historically focused on bright visible events associated with electron energies > 5 keV. Such aurorae arise from a “linear” or “ohmic” acceleration region wherein the characteristic energy (related to the potential drop) is proportional to the net number flux (related to the current). What is not well understood is how the parallel electric field is formed or how it is maintained. Such investigations require knowledge of energetic electron behavior during auroral formation and decay, when the electron characteristic energy is < 1 keV. Optical detection in this energetic regime is difficult, especially when bright arcs appear simultaneously within the field [Semeter *et al.*, 2001]. However, the importance of an auroral flux tube to dynamic magnetosphere-ionosphere coupling is not necessarily

indicated by luminosity or, equivalently, by the magnitude of the potential drop.

Consider, for example, the velocity distribution functions shown in Figure 1 taken from a 30 s interval of the PHAZE2 rocket flight of February 1997 [Arnoldy *et al.*, 1999]. The left column shows images of electron phase space density f as a function of parallel and perpendicular velocity. The center and right-hand columns are plots of downward differential number flux and energy flux, respectively, calculated from the following integrals:

$$\begin{aligned}\Phi_n &= \int \underbrace{v_{\parallel} f(v_{\parallel}, v_{\perp}) 2\pi v_{\perp} \partial v_{\perp} \partial v_{\parallel}}_{\phi_n} & (1) \\ \Phi_e &= \int \underbrace{\frac{1}{2} m (v_{\parallel}^2 + v_{\perp}^2) v_{\parallel} f(v_{\parallel}, v_{\perp}) 2\pi v_{\perp} \partial v_{\perp} \partial v_{\parallel}}_{\phi_e} & (2)\end{aligned}$$

where the quantities ϕ_n and ϕ_e have been plotted versus energy. Such plots are useful in visualizing which energetic regime is responsible for the majority of the number flux and energy flux. The integrated quantities Φ_n and Φ_e are shown in the upper right corner of the plots in Figure 1.

The aggregate luminosity of the aurora is proportional to Φ_e . One can see that as E_0 decreases, the net energy flux, and hence observed brightness, decreases in proportion. However, this is not the case for Φ_n , which remains roughly constant across the examples shown. Semeter *et al.* [2001] used these data in a combined optical-particle analysis to show that when E_0 becomes very low, a significant percentage of the field-aligned current is still carried by the suprathermal population, which becomes increasingly dominated by cold ambient electrons. With respect to understanding dynamic coupling between the magnetosphere and the auroral ionosphere, the observational bias toward bright aurora is physically unjustified.

The observational challenge is to devise a scheme whereby precipitation in the linear ($\gtrsim 1$ keV) and non-linear ($\lesssim 1$ keV) regimes may be imaged simultaneously. We desire the optical analog to the logarithmic sensitivity of a typical auroral electron detector. The logarithmic spacing of energy channels on rocket-borne electrostatic analyzers, for example, has persisted because of the early detection of field-aligned

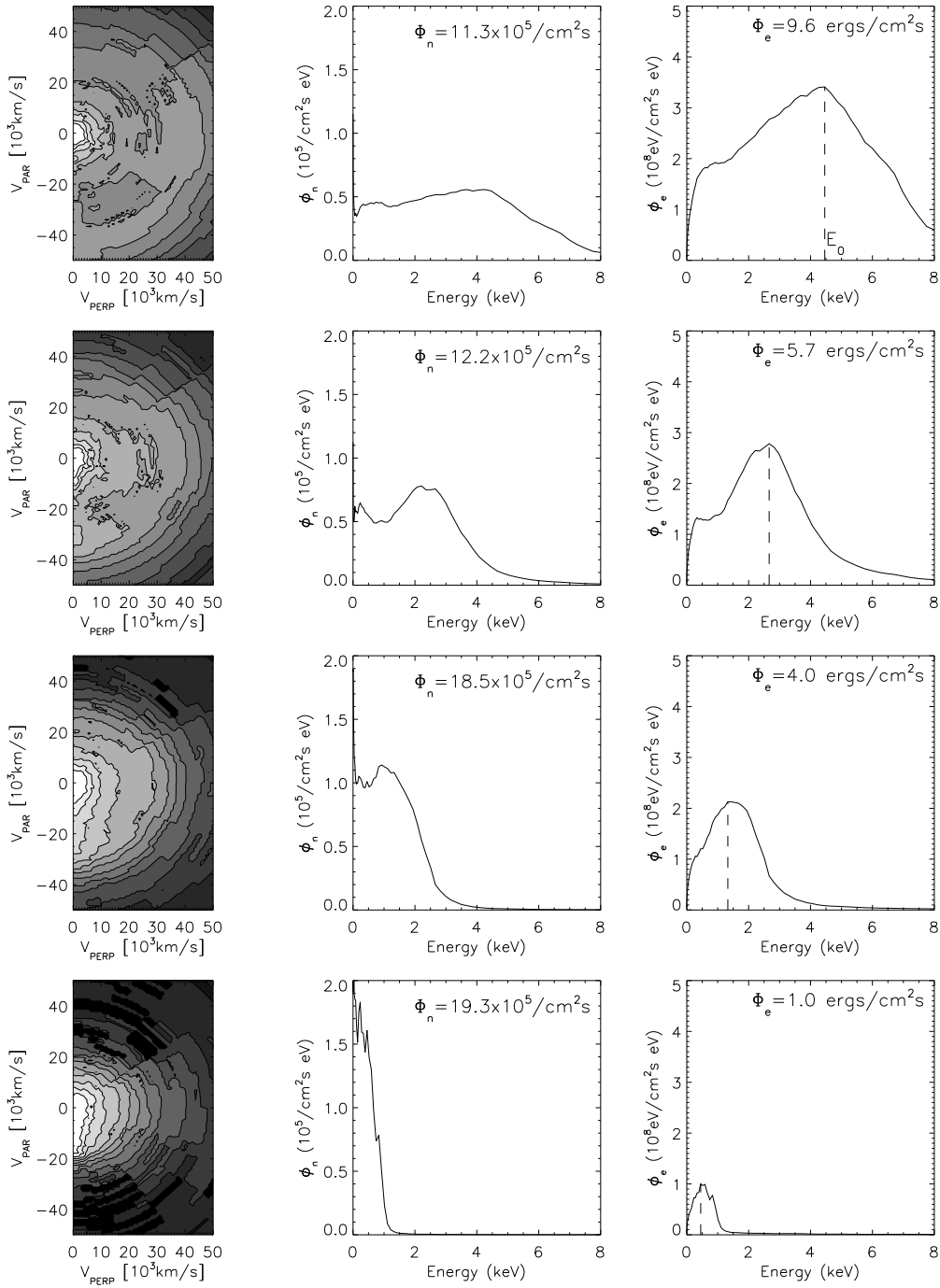


Figure 1. Velocity distribution functions for electron aurora recorded during a 30 s interval of the PHAZE2 rocket flight. The aggregate luminosity is proportional to Φ_e while the field-aligned current is proportional to Φ_n .

bursts [e.g., *Arnoldy*, 1985], and the acknowledgment that low-energy electron populations may play a key role in auroral formation [*Johnstone and Winningham*, 1982]. An analogous optical detection scheme requires that we exploit the wavelength-specific response of the thermosphere to precipitating energetic electrons.

3. Thermospheric response to auroral electrons

For incident electron energies greater than a few keV, the auroral spectrum is dominated by the oxygen green line at 5577Å and by the band systems of N_2 and N_2^+ , with the total luminosity proportional to net energy flux. As E_0 of the electron beam decreases, the higher altitude emissions of O and O^+ become increasingly significant. The change in spectral distribution reflects changes in the balance among electron penetration depth, species density, and thermospheric quenching, effects which can be modeled numerically from first principles. Given a model of the neutral atmosphere and an incident electron population in the form of $f(v_{\parallel}, v_{\perp})$, the optical response of the thermosphere can be written canonically as the inner product of a photon production model and the incident energy spectrum – that is,

$$Q_{\lambda}(z) = \int_{\text{all } E} q_{\lambda}(E, z) \phi_n(E) \partial E, \quad (3)$$

with ϕ_n the differential number flux and q_{λ} the production of photons at wavelength λ as a function of energy and altitude.

Figure 2 shows $Q_{\lambda}(z)$ for four prominent auroral emission lines calculated using the electron transport and degradation model of *Lummerzheim and Lilensten* [1994]. The color-coded curves show how the volume emission rate varies with characteristic energy (indicated in the legend to the left). Each profile was calculated for a Gaussian incident energy spectrum with a full-width at half-maximum of 10% and net energy flux of 1 mW/m². This narrow spectrum approximates a monoenergetic beam of electrons at the indicated energy, and the curves represent the optical response functions. An individual curve may be a poor model for an auroral emission profile but, since Eq. (3) is linear

in ϕ_n , the thermospheric response to a true auroral distribution function can be approximated by a superposition of these monoenergetic response functions. This is precisely what is done in a so-called CARD analysis [*Brekke et al.*, 1989], where ϕ_n is estimated from a set of model production profiles and measured E -region ionization rates by inverting a matrix form of Eq. (3) (i.e., $\phi_n = \mathbf{q}^{-1}\mathbf{Q}$).

As the optical analog to CARD, Figure 2 gives a set of “eigen-profiles” which reveal the sensitivity of the optical spectrum to various energetic regimes. As expected, the N_2^+ 4278 emission increases in magnitude and decreases in altitude with increasing energy. The other emissions shown arise from excited states of atomic oxygen, and are all anticorrelated with incident energy. For this reason, these emissions are not generally used in correlative studies of energetic auroral electrons. However, this anticorrelation can be advantageous when one wishes to study weak auroral precipitation. The oxygen 6300Å emission has long been used in this capacity, but is of limited use in studying dynamical aurora because of its 120 s radiative lifetime. Both the prompt emission of O 8446 and the O^+ 7320,7330 doublet (with a 5.8 s radiative lifetime) appear to be better choices in this regard. (For a detailed discussion on the auroral spectrum see *Chamberlain* [1961] and *Vallance-Jones* [1974].)

The photometric brightness of these spectral features in the magnetic zenith can be estimated from the curves of Figure 2 under certain assumptions of the incident energy spectrum (note that the actual “apparent brightness” requires a model for atmospheric scattering, which will be ignored in the present discussion). Figure 3a shows the results of direct integration. The constraint that $\Phi_e = 1$ mW/m² for each profile is manifested in the relatively constancy of 4278, which is a proxy for energy flux. In real aurora, Φ_e and E_0 are known to be correlated, so Figure 3a gives an unrealistic impression of the dependence of spectral brightness on E_0 . Measurements have shown that $\Phi_e \propto E_0^{\gamma}$ in high-energy aurora with $\gamma = 1.5 - 2$ [*Lyons et al.*, 1979; *Christensen et al.*, 1987]. The moderate to low energy distribution functions of Figure 1, on the other hand, are better modeled by $\gamma = 1$. Although the choice of γ is not crucial to the results of this work, $\gamma = 1$ will be

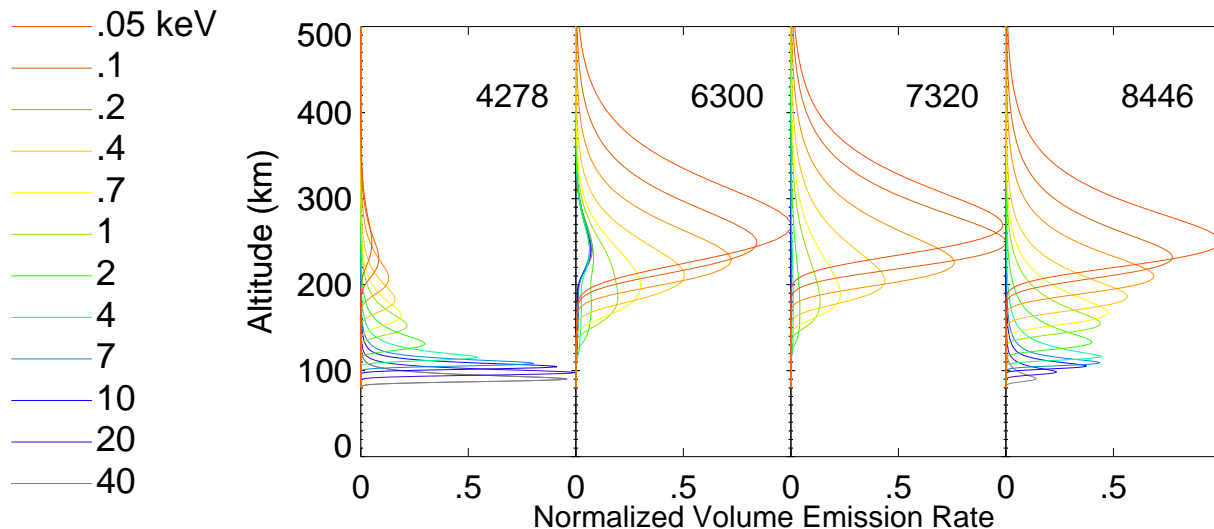


Figure 2. Modeled volume production profiles due to monoenergetic incident electron beams for four prominent auroral emissions.

assumed.

Figure 3b shows the modeled spectral brightnesses assuming $\Phi_e \propto E_0$. The anticipated linear increase in 4278 for increasing energy is now seen. The sensitivity of 4278/6300 to characteristic energy is manifested in the divergence of the two lines as energy decreases. Note that 7320 and 8446 also diverge from 4278 for energies less than a few keV. This behavior will be exploited in Section 5.

Note also that Figure 3 refers to the auroral spectrum at a single point in the magnetic zenith. However, we endeavor here to understand the relationship between the auroral energy spectrum and its spatial and temporal variability. We now describe an instrument and analysis framework for multispectral studies of the aurora.

4. Simultaneous multispectral imager

With respect to the goal of characterizing the primary electron beam, the auroral spectrum can be considered redundant. For example, emissions resulting from direct impact with N_2 are, to a good approximation, proportional to one another. In the case of individual bands within a band system (e.g., First Positive, Second Positive, First Negative) the proportion-

ality is described by Franck-Condon factors, and is nearly exact. For the emissions of atomic oxygen, the situation is somewhat more complicated owing to the very low excitation energies and smaller required penetration depth. In the case of 6300, there is also a certain hysteresis caused by the 120 s radiative lifetimes. Nonetheless, the full spectral detail afforded by dispersion-based instruments is not necessary, and the four wavelengths discussed in Section 3 provide sufficient information to infer much about the evolution of the incident energy spectrum.

As such, the Simultaneous Multispectral Imager was designed to provide two-dimensional images at four preselected wavelengths simultaneously. The SMI represents a modification to the standard monochromatic imaging system used extensively in experimental aeronomy [e.g., Baumgardner *et al.*, 1993]. The optical layout is illustrated schematically in Figure 4. The front objective is a 100 mm f/1.4 achromat. A field stop is placed at its focus to define a square focal plane with 22° diagonal field of view (~ 40 km at a typical E -region auroral altitude of 100 km). The beam is then collimated using a field lens and 300 mm f/2.8 achromat. The collimated beam is incident on a mosaic of square interference filters, each with identical dimensions. The mosaic is sized such that the 12 cm collima-

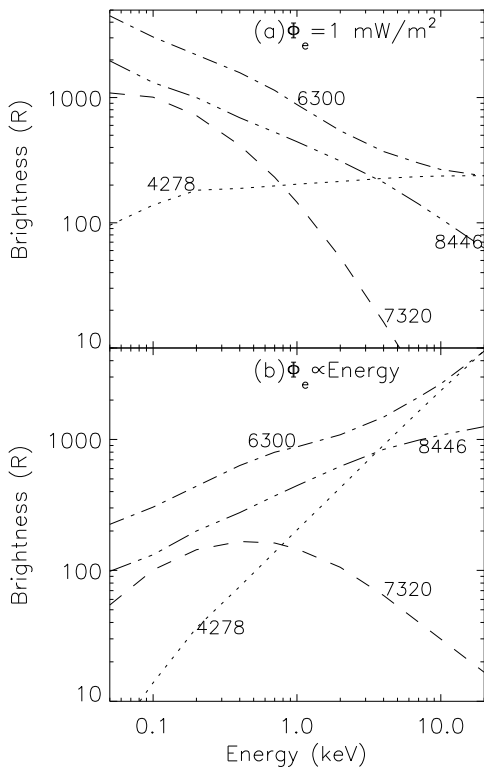


Figure 3. Spectral brightness vs. characteristic energy for (a) a constant energy flux of 1 mW/m^2 , and (b) energy flux proportional to characteristic energy.

tor output aperture is exactly inscribed in the square mosaic. The individual filters are removable so that various combinations of four spectral bands can be selected, depending on the objectives of the investigation.

In a standard monochromatic imager, a reimaging lens is placed behind the interference filter to produce the final image which, in this case, would consist of a mixture of the signals transmitted by the four filters. In the SMI, a wedge prism is placed behind each filter to divert the transmitted beam outward from the center by a small angle (5.44°). Figure 5 shows a schematic drawing of a wedge prism. The center of the prism array is at the top at the thinnest point of the wedge. When properly configured, the reimaged focal plane will contain four copies of the original scene, each corresponding to a different filter.

This design concept suggests a fundamental trade-off between spectral and spatial resolution. A greater

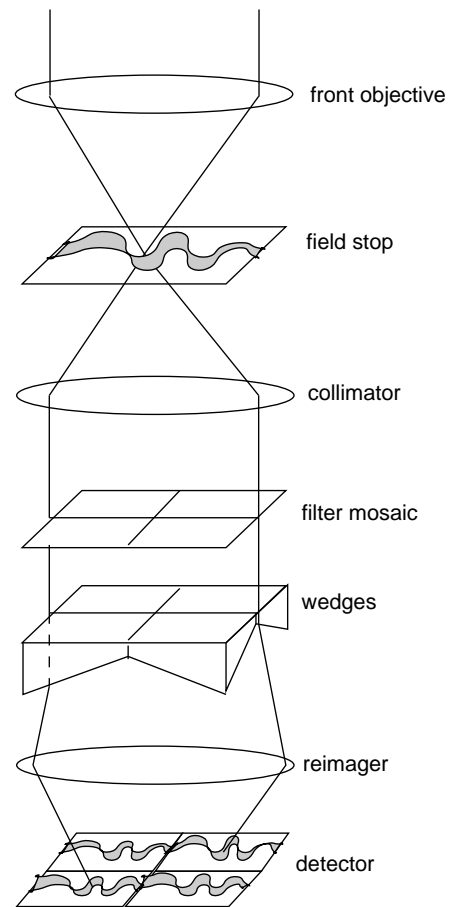


Figure 4. Optical schematic for the SMI.

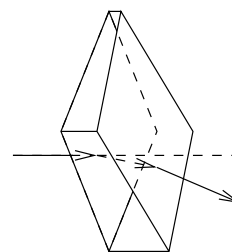


Figure 5. Wedge prism. Four such elements comprise the SMI wedge prism array.

number of wavelengths could be imaged by increasing the number of filters in the mosaic, decreasing the reimager focal length (i.e., reducing the image size), and adjusting the number and angles of the wedge elements. In principle, an arbitrary number of spectral images could be arranged on a single array detector in this way. The spatial resolution decreases as the number of wavelengths increases, but the effective system speed remains constant.

The SMI detector consists of a microchannel plate image intensifier coupled to a CCD via a fiber optic taper. Both the intensifier gain and the CCD exposure time can be adjusted in software. The CCD is a 576×768 rectangular array. With an approximate point spread function of three pixels, the effective spatial resolution at 100 km altitude is ~ 300 m.

Filter specifications

In the SMI, we seek to isolate individual features in the auroral spectrum. This requires narrow band filters fabricated to careful specifications. The transmission characteristics of an interference filter are a strong function of the beam incident angle. For angles less than 5° , the center wavelength shifts by $\sim 1 \text{ \AA}/\text{degree}$. The maximum incident angle produced by the 300 mm collimator is 3.8° . Under this constraint, an interference filter with a transmission full-width at half-maximum (FWHM) of 10 \AA and with center wavelength (CWL) shifted 2 \AA towards the red will transmit the selected wavelength optimally over the entire range of incident angles (i.e., the entire field of view), while minimizing background contribution.

Table 1 lists the salient features of the current SMI filter set. The desired spectral feature and its source species are indicated in the last two columns. The CWL of the H_β filter was blue-shifted by 6 \AA to account for the average observed Doppler shift. The larger FWHM of the 7325 filter is to include both lines of the 7320,7330 doublet.

Throughout the remainder of this work, we refer to both the filter and the associated image by the CWL. This is to clarify that, in general, a spectral imager images wavelength bands, and not individual spectra lines. In the case of 4278, the filter captures only a portion of the (0,1) band in the First Negative system. The

TABLE 1. CHARACTERISTICS OF CURRENT SMI FILTERS

Filter Specification			
CWL	FWHM	Spectral Feature	Source
4278	12	4278	N_2^+ (1N)
4855	15	4861	H_β
7325	25	7320,7330	O^+
8446	12	8446	O

Table values are in Angstroms. CWL = center wavelength of filter. FWHM = full width at half maximum of filter.

calibrated brightness will be proportional to the integrated band intensity.

Figure 6 gives an example of multispectral data acquired by the SMI (right panel) and allsky camera (middle and left panels). These are raw images recorded at Sondrestrom, Greenland, for a weak stable auroral event in the magnetic zenith. The 6300 and 4278 images were recorded sequentially at the Universal time (UT) and exposure time shown in the upper left corner. The SMI image was recorded with a 10 s exposure at the UT indicated in the center. Each quadrant contains an image of the same field through the filter with CWL as indicated. The white square in the allsky images is the projected SMI field of view. In this case, the raw signals recorded by the 8446, 4278, and 7325 filters were of similar magnitude, while no signal at 4861 is immediately discernable.

5. Multispectral analysis at 7325Å and 4278Å

There are many ways to apply such data, but let us consider for the present one specific application, that of characterizing behavior of auroral structures during changes in characteristic energy of the incident electron beam. This requires simultaneous measurements of emissions whose production rates peak at different electron energies. Historically, this has been accomplished using measurements of N_2^+ 4278 and O 6300 from a photometer or spectrograph. But without the concomitant spatial information, one cannot resolve whether a change in energy is caused by convection of

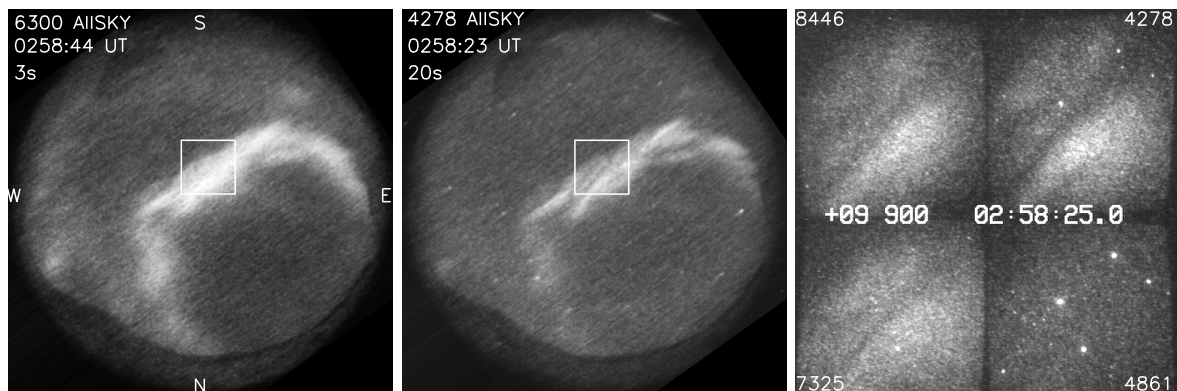


Figure 6. Sample raw data from the Sondrestrom Allsky camera (left and middle images) and the SMI (right image).

a spatially varying source, or temporal variation in a stationary source, nor can one investigate relationships between auroral morphology and the optical spectrum.

Because we are interested in dynamic aurora, we will use images at 7325 instead of the usual 6300 measurements. The O^+ 7320,7330Å doublet (hereafter referred to as 7320) originates in the F region and depends on a substantial flux of low-energy primary electrons. As such, it is normally quite weak in energetic aurora. But, as will be demonstrated, 7320 can provide a high-resolution diagnostic for low-energy precipitation structures. The main disadvantage is contamination by the (5,3) band of the N_2 First Positive system.

To understand how properly to interpret SMI images at 7325, consider Figure 7, which shows three examples of the auroral spectrum in this wavelength regime (from *Sivjee and Shen* [1997]). The transmission curve of the 7325 filter is shown as the shaded curve. There are essentially two auroral sources within the filter pass band: O^+ 7320 and the $N_2(5,3)$ First Positive band. Which of these features dominates depends on the auroral conditions. In normal visible aurora (Figure 7a), the image will be dominated by the N_2 source (the two broad humps). For weak precipitation in the cusp (Figure 7b), the O^+ source is of comparable magnitude (the narrow peaks under the filter curve), and for the magnetic cloud event (Figure 7c), the O^+ source was dominant.

As a consequence of the competing sources, the 7325 filter has the interesting property of continuing to

provide a signal down to very low energies, when the N_2 and N_2^+ band emissions are no longer detectable. What is needed is a means of separating the contribution from each source. Simultaneous images at 4278Å offer one solution.

The brightness transmitted by a filter identified by CWL λ_0 is related to spectral intensity by

$$B_{\lambda_0} = \int_{-\infty}^{+\infty} T_{\lambda_0}(\lambda) S(\lambda) \partial\lambda, \quad (4)$$

where T_{λ_0} refers to the transmission of a filter with CWL λ_0 , and S is the source function in $R/\text{Å}$. There is only one auroral source within the 4278 filter pass band, so that

$$B_{4278} = \int_{-\infty}^{+\infty} T_{4278}(\lambda) [S_{N_2^+(1N)}] \partial\lambda \quad (5)$$

$$= B_{N_2^+(1N)} \quad (6)$$

where $B_{N_2^+(1N)}$ is proportional to the brightness of the N_2^+ First Negative system.

Similarly, the brightness transmitted by the 7325 filter can be written

$$B_{7325} = \int_{-\infty}^{+\infty} T_{7325}(\lambda) [S_{O^+} + S_{N_2(1P)}] \partial\lambda \quad (7)$$

$$= B_{O^+} + B_{N_2(1P)} \quad (8)$$

where B_{O^+} refers to the integrated intensity of O^+ (7320,7330) doublet, and $B_{N_2(1P)}$ is the transmitted portion of the (5,3) band of N_2 First Positive.

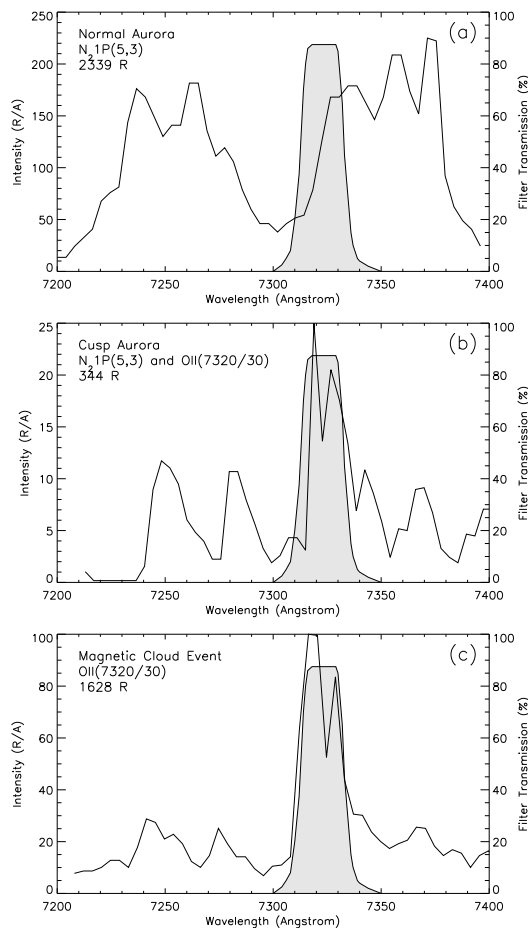


Figure 7. Three examples of the near infrared auroral spectrum (from *Sivjee and Shen [1997]*) The transmission curve for the SMI 7325 filter is shown in gray.

To a good approximation, $B_{N_2(1P)}$ and $B_{N_2^+(1N)}$ are proportional to one another in the aurora. Both are prompt emissions produced directly by secondary electron impact on N_2 (the First Negative bands are ~ 19 eV above the ground state of N_2 , the First Positive bands ~ 7 eV). The distribution of secondaries at E -region altitudes is relatively insensitive to the mean energy of the primary beam. As such, the energy distribution of the secondaries scales with energy flux, leading to the proportionality of the band systems [*Chamberlain, 1961, ch. 5*]. We can therefore write $B_{N_2(1P)} \approx K B_{N_2^+(1N)}$, where K is a constant (note that K depends on the filter transmission curves and thus has no direct physical interpretation). The transmitted brightnesses are related to the spectral brightnesses by

$$\frac{B_{7325}}{B_{4278}} = \frac{B_{O^+}}{B_{N_2^+(1N)}} + K. \quad (9)$$

For very bright aurora, $B_{N_2^+(1N)} \gg B_{O^+}$ such that $B_{7325}/B_{4278} \approx K$. Thus, the value of K can be estimated from the data themselves. At lower energies, changes in characteristic energy will produce an increase in B_{7325}/B_{4278} as B_{O^+} increases. Thus, Eq. (9) also reveals how this filter scheme serves to extend the sensitivity and expand the dynamic range to lower electron energies.

There are a few interesting properties to note about K : (1) because it is proportional to the ratio of two emissions of the same N_2 parent species K is independent of thermospheric composition; (2) K is not affected by altitude variability between oxygen and nitrogen emissions for the same reason; and (3) if we are concerned only with detecting relative changes in characteristic energy, or simply acquiring images of the aurora at lower characteristic energies, then we need not be concerned about absolute calibration, since the calibration constant is included in K .

These effects can be modeled using the monoenergetic emission profiles of Figure 2. Figure 8a shows once again the 4278 and 7320Å brightness as a function of electron energy (assuming $\Phi_e \propto E_0$ as before). The sum of these sources, shown by the solid curve, simulates qualitatively the brightness observed through the 7325 filter as a function of energy (i.e., B_{7325} in (Eq. 9) assuming $K = 1$). Figure 8b simulates the

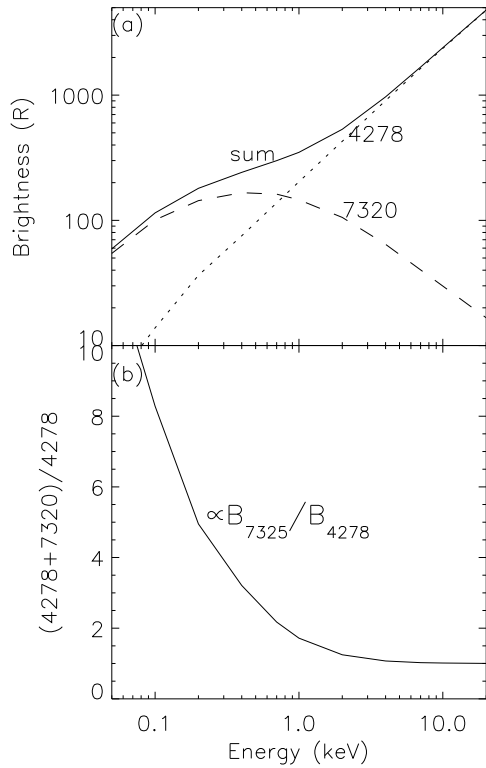


Figure 8. (a) Modeled spectral brightness vs. E_0 at 7320Å and 4278Å. (b) Estimated qualitative response of B_{7325}/B_{4278} vs. E_0 .

ratio B_{7325}/B_{4278} versus energy. As suggested by Eq. (9), the ratio approaches a constant as the auroral energy increases. At lower energies, we should expect a sharp increase in this ratio below ~ 1 keV.

The sensitivity of the auroral spectrum in the 7320 to 7330Å band to incident electron energy has been demonstrated both observationally (Figure 7) and theoretically (Figure 8). Unlike the 4278/6300 ratio, B_{7325}/B_{4278} is only sensitive to E_0 below ~ 1 keV. While not providing the same range of sensitivity as the classic “red to blue” ratio, the proposed technique provides a means of sensing changes in E_0 at low energies, as well as a means of effectively detecting the discrete aurora associated with < 1 keV electrons.

6. Results

The technique proposed in Section 5 is now demonstrated using data acquired by the SMI in a campaign at Sondrestrom, Greenland, in February–March of 2000. The images have been calibrated to Rayleighs using a low brightness source. The peak brightness of the features in the images will be indicated as required.

6.1 Fine structure

Figures 9 and 10 show image sequences at 4278 and 7325. The magnetic zenith is indicated by the square symbol. Both sequences were recorded at .3 s resolution. The considerable speckle (especially in the 7325 images) highlights the trade-off between intensifier gain and exposure time in capturing spectral images through narrowband filters. Figure 9 shows a developing auroral structure. There is little apparent motion during the 8 s interval shown. Figure 10, recorded ~ 3 min later, shows an evolving small-scale vortex, which reached a peak brightness of ~ 1600 R at both 4278 and 7325. This structure is much narrower and more dynamic than the structure in Figure 9.

Figures 11 and 12 show the zenith brightnesses versus time at 4278, 7325, and 8446, as well as the 7325/4278 ratio in the time intervals of these events. Figure 11 (associated with Figure 9) shows a clear decrease in the 7325/4278 ratio from 0254:20 to 0254:30 UT. Comparing this result with the image sequence indicates that this decrease was the result of a true ener-

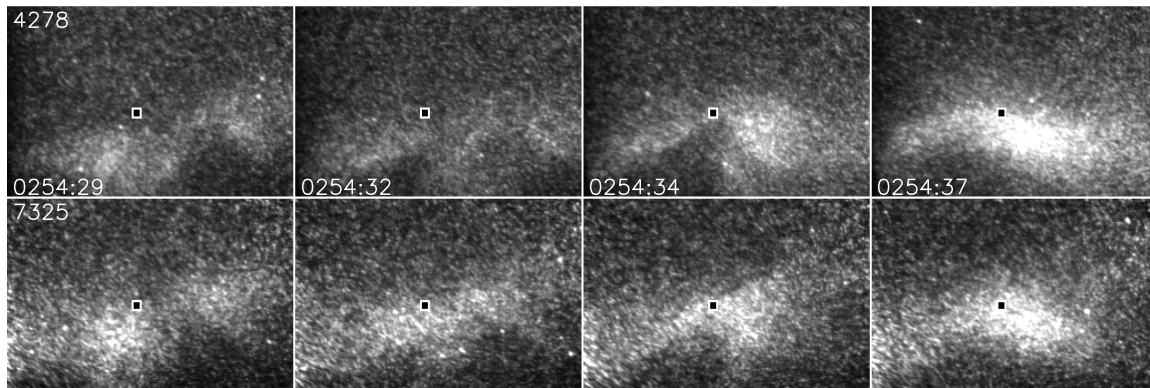


Figure 9. SMI measurements at 4278Å and 7325Å indicating a time change in characteristic energy.

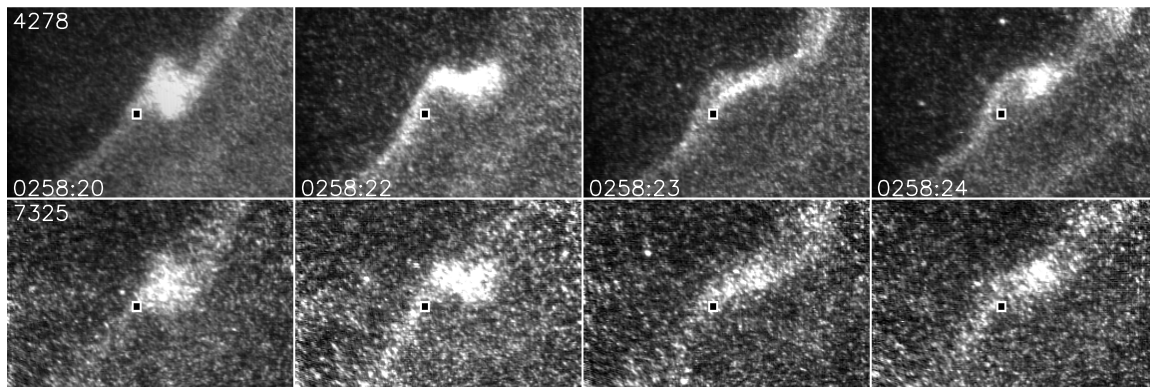


Figure 10. SMI measurements at 4278Å and 7325Å of an auroral vortex structure appearing in a high-energy discrete auroral arc.

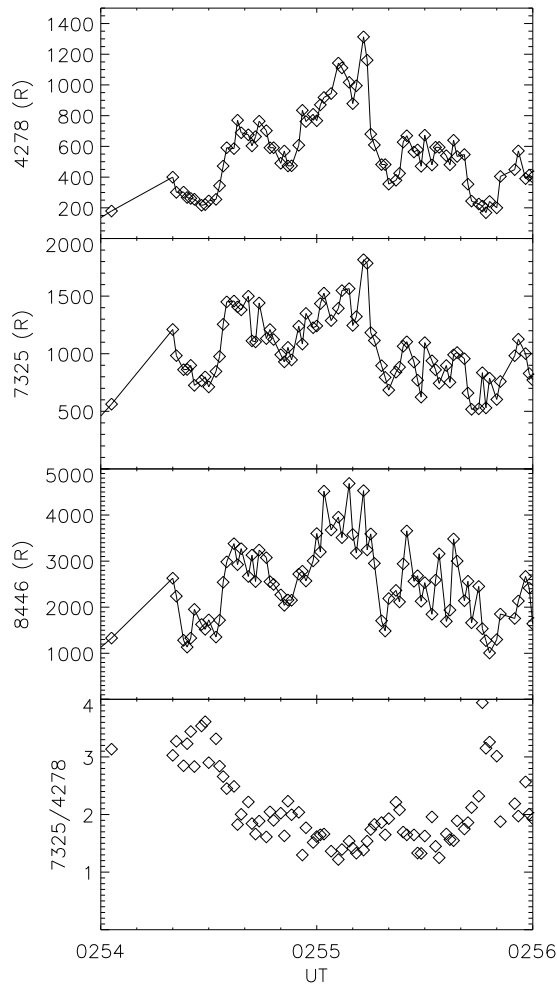


Figure 11. Observed brightness for Figure 9 event along with 7325/4278 ratio. Change in ratio is presumably the result of change in characteristic energy of the source.

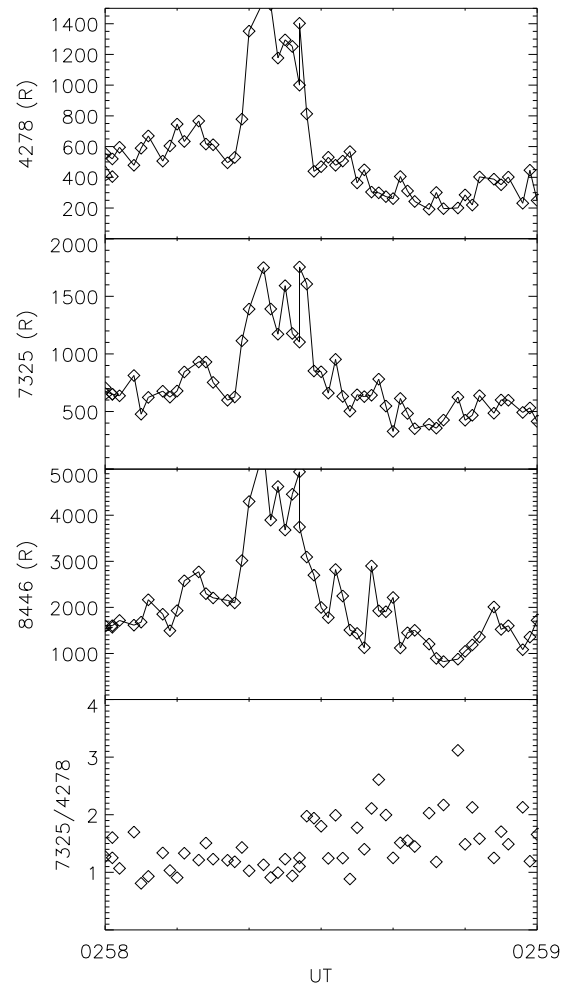


Figure 12. Observed brightness for Figure 10 event along with 7325/4278 ratio. Ratio is constant through large changes in spectral brightness, presumably indicating a change in number flux at a constant characteristic energy.

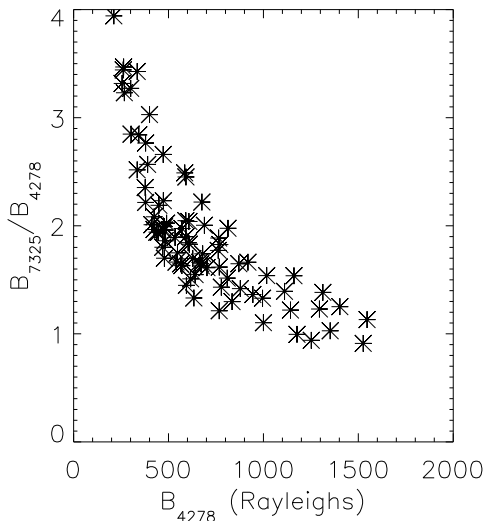


Figure 13. Observed 7325/4278 ratio as a function of 4278 brightness. The trend closely matches Figure 8b.

gization of a stationary auroral form, and not the result of convection of a spatially varying source. Figure 12 (associated with Figure 10), on the other hand, shows a relatively constant but smaller 7325/4278 ratio from 0258:00 to 0258:30 UT. This aurora is associated with a higher characteristic energy, as manifested in the lower average value of the 7325/4278 ratio. Also note the constancy of this ratio despite considerable variability in the brightness curves, especially prior to 0258:30 UT.

We can also investigate whether these observations are qualitatively consistent with the predictions of Figure 8b. In Figure 13, B_{7325}/B_{4278} has been plotted against B_{4278} for the two events in Figures 11 and 12. To insure adequate signal-to-background, only measurements with $B_{7320} > 800$ R have been considered. The trend can be seen to match Figure 8b quite closely. From these measurements, one can also see that K , the asymptotic value of B_{7325}/B_{4278} for large B_{4278} , appears to be ~ 1 for this configuration.

6.2 Arc genesis

One of the important benefits of multispectral imaging at these wavelengths is to extend the effective sensitivity to lower energies, thus allowing access to the

low energy velocity distribution functions discussed in Section 2. Figure 14 shows allsky camera images at 6300 (left) and SMI images at 7325 and 4278 (center and right) for a nascent auroral arc. Universal time is indicated in the upper right for each sequence. The inset box in the 6300 images corresponds to the SMI field of view. The square symbol in the SMI images shows the magnetic zenith. The exposure time for both SMI and allsky images was 10 s.

The 6300 sequence shows the formation of an arc near the zenith which expands toward the southwest. Under this spatial–spectral resolution, the nascent arc appears as an expanding sheet. However, in the SMI 7325 images, the same arc appears first as a series of separate structures that remain disconnected until 0430:14 UT. The 10 s exposure certainly smooths out the true detail, but one can surmise that these structures are individual auroral rays, normally associated with energetic events.

Note that no 4278 emission is detectable in this sequence (right panels). For this configuration, the sensitivity at 4278 was 20 R. The very large 7325 to 4278 ratio in this sequence indicates that the 7325 images are indeed dominated by emissions of O^+ 7320 and not N_2 First Positive. The consequences of such measurements will be explored in detail in a future work.

7. Summary and future work

We have described a multispectral imager and an associated multispectral imaging framework, for the study of small-scale spatial–spectral variability in the discrete aurora. The SMI acquires images at four pre-selectable wavelengths simultaneously over a 20° field of view and with ~ 300 m resolution at E -region altitudes. The current filter set is summarized in Table 1.

There are many ways to apply such data, both in purely aeronautical studies and studies of auroral electrodynamics. This work has focused on the particular goal of using multispectral imaging to increase the effective sensitivity and dynamic range of the passive imaging process with respect to the incident energy spectrum. A technique has been proposed that uses the simultaneous images at 7325Å and 4278Å to detect both very low (< 1 keV) and very high energy (> 5 keV)

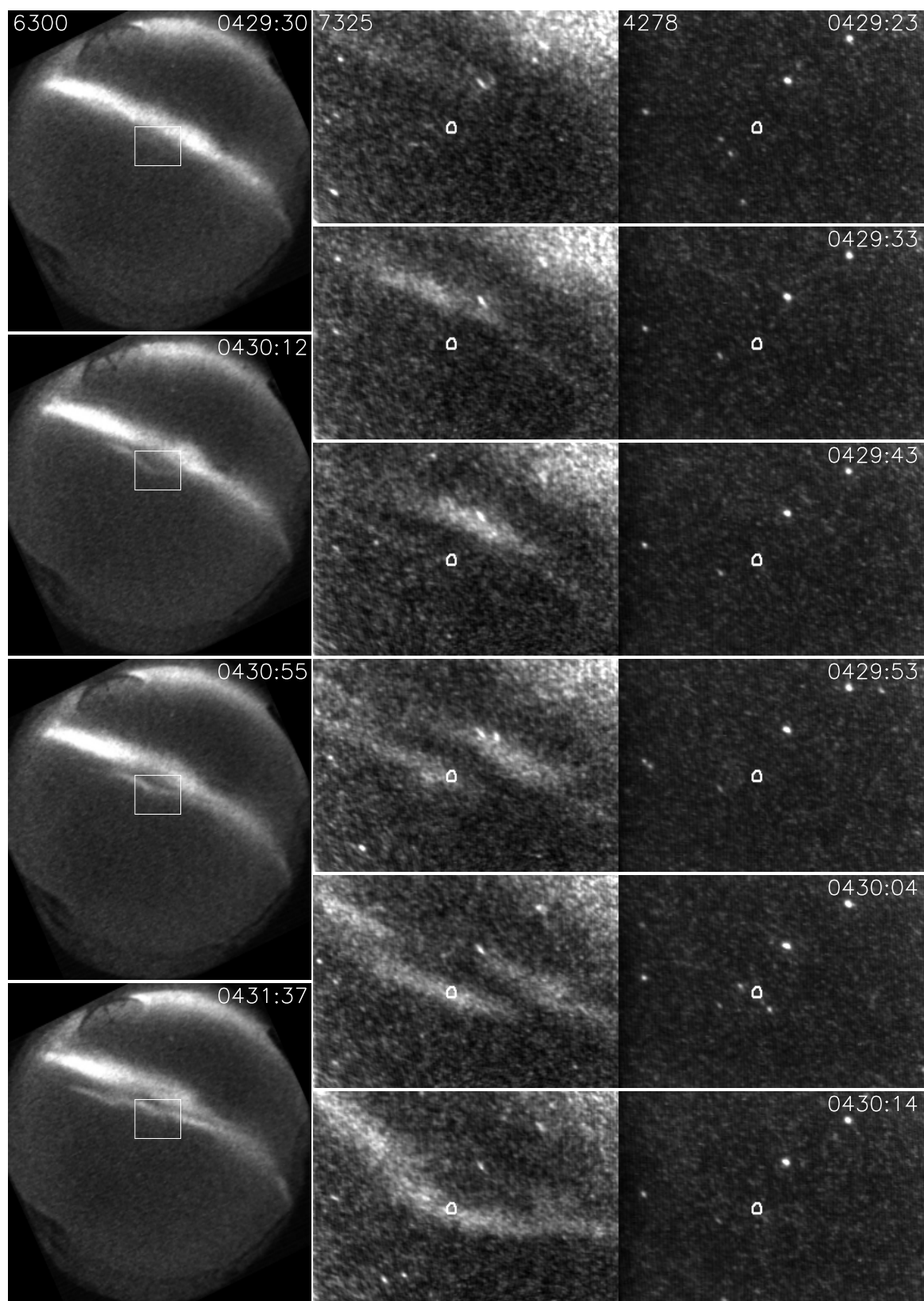


Figure 14. Allsky image at 6300Å and SMI images at 7325Å and 4278Å of a forming auroral arc.

precipitation simultaneously. The technique exploits the pseudo-logarithmic sensitivity of atomic oxygen emissions in the auroral optical spectrum and, as such, represents an optical analog to the logarithmic spacing of energy channels on auroral particle detectors.

Future work will involve more detailed modeling of the SMI image acquisition using synthetic auroral spectra. SMI measurements will also be combined with simultaneous measurements of E -region ionization by the Sondrestrom incoherent-scatter radar.

Acknowledgment. We would like to acknowledge Werner Lieb at the Max Planck Institute for Extraterrestrial Physics for his role in developing the SMI. We thank the Sondrestrom site crew for campaign support. Funding for the SMI was provided by the Max Planck Society. The Sondrestrom campaign was supported by NSF grant ATM-9813556.

References

- Arnoldy, R. L., Low-altitude field-aligned electrons, *J. Geophys. Res.*, *90*, 8445, 1985.
- Arnoldy, R. L., K. A. Lynch, and J. B. Austin, Energy and pitch angle-dispersed auroral electrons suggesting a time-variable, inverted-V potential structure, *J. Geophys. Res.*, *104*, 22613, 1999.
- Baumgardner, J., B. Flynn, and M. Mendillo, Monochromatic imaging instrumentation for applications in aeronomy of the Earth and planets, *Opt. Eng.*, *32*(12), 3028, 1993.
- Brekke, A., C. Hall, and T.L. Hansen, Auroral ionospheric conductances during disturbed conditions, *Ann. Geophys.*, *7*(3) 269–280, 1989.
- Chamberlain, J.W., *Physics of Airglow and Aurora*, Academic, New York, 1961.
- Christensen, A.B., L.R. Lyons, J.H. Hecht, G.G. Sivjee, R.R. Meier, and D.G. Strickland, Magnetic field-aligned electric field acceleration and the characteristics of the optical aurora, *J. Geophys. Res.*, *92*(A6) 6163–6167, 1987.
- Hallinan, T.J., Auroral Spirals 2. Theory, *J. Geophys. Res.*, *81*(22), 3959–3964, 1976.
- Johnstone, A. D., and J. D. Winningham, Satellite observations of suprathermal electron bursts, *J. Geophys. Res.*, *87*, 2321, 1982.
- Lyons, L. R., D. S. Evans, and R. Lundin, An observed relation between magnetic field aligned electric fields and downward electron energy fluxes in the vicinity of auroral forms, *J. Geophys. Res.*, *84*, 457, 1979.
- Lummerzheim, D., and J. Lilensten, Electron transport and energy degradation in the ionosphere: Evaluation of the numerical solution, comparison with laboratory experiments and auroral observations, *Ann. Geophys.*, *12*, 1039, 1994.
- Rees, M. H., and D. Luckey, Auroral electron energy derived from ratio of spectroscopic emissions, 1, Model computations, *J. Geophys. Res.*, *79*, 5181, 1974.
- Semeter, J., J. Vogt, G. Haerendel, K. Lynch, and R. Arnoldy, Persistent quasiperiodic precipitation of suprathermal ambient electrons in decaying auroral arcs, *J. Geophys. Res.*, in press, 2001.
- Sivjee, G. G., and D. Shen, Auroral optical emissions during the solar magnetic cloud event of October 1995, *J. Geophys. Res.*, *102* 7431 1997.
- Vallance-Jones, A., “Aurora,” *Astrophys. Monogr. Ser.*, vol. 9, D. Reidel, Norwell, Mass., 1974.
- Vogt, J., H.U. Frey, G. Haerendel, H. Hoefner, and J. Semeter, Shear velocity profiles associated with auroral curls, *J. Geophys. Res.*, *104*, A8, 1999.

J. Semeter, SRI International, 333 Ravenswood Avenue, Menlo Park, CA 94025. (Joshua.Semeter@sri.com)

This preprint was prepared with AGU’s L^AT_EX macros v5.01, with the extension package ‘AGU++’ by P. W. Daly, version 1.6b from 1999/08/19.